Original Article

MOLECULAR METABOLISM

Dysregulated transmethylation leading to hepatocellular carcinoma compromises redox homeostasis and glucose formation

Curtis C. Hughey [1,*], Freyja D. James [1,2], Zhizhang Wang [2], Mickael Goelzer [1], David H. Wasserman [1,2]

ABSTRACT

Objective: The loss of liver glycine N-methyltransferase (GNMT) promotes liver steatosis and the transition to hepatocellular carcinoma (HCC). Previous work showed endogenous glucose production is reduced in GNMT-null mice with gluconeogenic precursors being used in alternative biosynthetic pathways that utilize methyl donors and are linked to tumorigenesis. This metabolic programming occurs before the appearance of HCC in GNMT-null mice. The metabolic physiology that sustains liver tumor formation in GNMT-null mice is unknown. The studies presented here tested the hypothesis that nutrient flux pivots from glucose production to pathways that incorporate and metabolize methyl groups in GNMT-null mice with HCC.

Methods: $^{2}H/^{13}C$ metabolic flux analysis was performed in conscious, unrestrained mice lacking GNMT to quantify glucose formation and associated nutrient fluxes. Molecular analyses of livers from mice lacking GNMT including metabolomic, immunoblotting, and immunochemistry were completed to fully interpret the nutrient fluxes.

Results: GNMT knockout (KO) mice showed lower blood glucose that was accompanied by a reduction in liver glycogenolysis and gluconeogenesis. NAD^+ was lower and the NAD(P)H-to-$NAD(P)^+$ ratio was higher in livers of KO mice. Indices of NAD^+ synthesis and catabolism, pentose phosphate pathway flux, and glutathione synthesis were dysregulated in KO mice.

Conclusion: Glucose precursor flux away from glucose formation towards pathways that regulate redox status increase in the liver. Moreover, synthesis and scavenging of NAD^+ are both impaired resulting in reduced concentrations. This metabolic program blunts an increase in methyl donor availability, however, biosynthetic pathways underlying HCC are activated.

Keywords Intermediary metabolism; Metabolic flux analysis; NAD^+; Redox state; S-adenosylmethionine

1. INTRODUCTION

The incidence of liver cancer, of which hepatocellular carcinoma (HCC) is the primary form, is increasing in the United States [1—3]. This rise in newly diagnosed liver cancer is proposed to be, in part, the result of the high prevalence of metabolic diseases such as diabetes and obesity [1,2]. Dysregulated metabolism is an important contributor to the pathogenesis of cancer [4]. This metabolic reprogramming includes dysregulated nutrient uptake, metabolite mediated changes in cell function, and shifts in intracellular nutrient fluxes [5]. From the perspective of liver nutrient flux, experimental models suggest that impeding glucose production promotes HCC [6,7], while enhancing glucose production has the opposite effect [8,9]. It has been proposed that the reduction in hepatic glucose formation spares precursors for alternate metabolic and biosynthetic pathways that contribute to tumorigenesis [10,11]. Findings in humans with HCC support this hypothesis. For example, glucose production in response to gluconeogenic stimuli such as glucagon is diminished in patients with HCC [12]. Also, hypoglycemia has been reported as an early characteristic in a subset of individuals with HCC [13,14].

Of particular interest in the relationship between glucose control and HCC is the role of liver glycine N-methyltransferase (GNMT). GNMT, the most abundant liver methyltransferase, catalyzes a reaction whereby a methyl group from s-adenosylmethionine (SAM) is transferred to glycine forming sarcosine and s-adenosylhomocysteine (SAH) [15]. The main function of this enzyme is to maintain SAM homeostasis. In humans with HCC, liver GNMT can be greatly decreased [16,17]. Moreover, GNMT-null mice develop HCC by eight months of age [18—20] suggesting a causal role for impaired GNMT action and dysregulated SAM in tumorigenesis. We have previously shown that glucose formation is impaired in GNMT-null mice at 12 weeks of age prior to HCC [10]. This is associated with a dysregulated energy state in the liver which includes a reduction in NAD^+ [10,21]. The NAD^+-to-NADH ratio influences citric acid cycle (CAC) and gluconeogenic reactions [22,23] such that critically low NAD^+ availability would diminish glucose formation. Results also indicated that gluconeogenic

[1]Department of Molecular Physiology & Biophysics, Vanderbilt University, Nashville, TN, USA [2]Mouse Metabolic Phenotyping Center, Vanderbilt University, Nashville, TN, USA

*Corresponding author. Department of Molecular Physiology and Biophysics, Vanderbilt University, 823 Light Hall, 2215 Garland Ave, Nashville TN, 37232 USA. E-mail: curtis.hughey@vanderbilt.edu (C.C. Hughey).

Received February 2, 2019 • Revision received February 18, 2019 • Accepted February 20, 2019 • Available online 25 February 2019

https://doi.org/10.1016/j.molmet.2019.02.006

precursors were being diverted to pathways that counter the elevation in SAM [10]. These SAM utilization pathways are biosynthetic in nature and are pro-tumorigenic.

As noted above, we have previously shown that impaired glucose formation in 12-week-old GNMT-null mice occurs prior to the appearance of liver tumor formation. Given this, we hypothesized that the reduced glucose production owing to a shift in precursor fate is key in promoting and maintaining liver tumorigenesis in GNMT-null mice. Here we directly test whether glucose formation is impaired in 44-week-old GNMT knockout (KO) mice with HCC to further assess whether this metabolic pathway underlies tumorigenesis in the absence of GNMT. $^{2}H/^{13}C$ metabolic flux analysis (MFA) of nutrients was combined with metabolomic analysis in conscious, unrestrained GNMT KO mice and wild-type (WT) littermates under post-absorptive conditions. The results show the lack of GNMT reduces glucose production from glycogen and gluconeogenic sources. Evidence from molecular and metabolomic analyses lead to the conclusion that reduced glucose production is coupled to impaired NAD^{+} synthesis and salvage. Results show a decline in NAD^{+} availability may diminish glucose production directly and/or by redirecting flux of glucose precursors to pathways that regulate liver redox state and tumorigenesis. These pathways include de novo glutathione synthesis and the pentose phosphate pathway.

2. MATERIAL AND METHODS

2.1. Animals

Vanderbilt University Animal Care and Use Committee approved mouse procedures. Male, mice with a global KO of GNMT and WT littermates [10,24] had ad libitum access to food (PicoLab® Laboratory Rodent Diet 5L0D, Purina, Richmond, IN, USA) and water. The mice were housed with natural soft cellulose bedding (BioFresh™ Comfort Bedding, Ferndale, WA, USA) in a humidity- and temperature-controlled room on a 12-hour light/dark cycle. Mice were studied at 44 weeks of age unless otherwise stated.

2.2. Body composition

Body composition was determined by using a mq10 nuclear magnetic resonance analyzer (Bruker Corporation, Billerica, MA, USA) in 43-week-old, male mice.

2.3. Surgical procedures

Mice receiving stable isotope infusions had vascular catheterization surgeries performed as previously described [25] at 43 weeks of age. Seven days of postoperative recovery was provided before stable isotope infusion studies were completed. Mice were individually housed during the postoperative recovery period.

2.4. Stable isotope infusions

Access to food and water was prevented during the first hour of the light cycle. Three hours into the fast, the exteriorized ends of the implanted catheters were connected to infusion syringes via a two-channel swivel. Following an hour acclimation, an 80 μl arterial blood sample was obtained to determine natural isotopic enrichment of plasma glucose. Venous infusions were performed as previously described in conscious, unrestrained mice [10,26]. In brief, a bolus of $^{2}H_2O$ (99.9%)-saline solution was infused over the course of a 25-minute period to achieve 4.5% enrichment of body water. [6,6-$^{2}H_2$] glucose (99%) solubilized in the $^{2}H_2O$-saline bolus was delivered as a prime (440 μmol kg^{-1}). Subsequently, a continuous [6,6-$^{2}H_2$]glucose (4.4 μmol $kg^{-1}\cdot min^{-1}$) infusion was started. An intravenous administration of [$^{13}C_3$]propionate (99%, sodium salt) was delivered as a primed (1.1 mmol kg^{-1}), continuous (0.055 mmol $kg^{-1}\cdot min^{-1}$) infusion starting two hours following the $^{2}H_2O$ bolus and [6,6-$^{2}H_2$] glucose prime. From 90 to 120 min after initiating the [$^{13}C_3$]propionate bolus (7.5—8 h of fasting), 100 μl arterial samples were obtained every 10 min (four samples in total) and stored at −20 °C. Following the final arterial sample, mice were sacrificed via cervical dislocation. Tissues were excised, freeze-clamped, and stored at −80 °C. The eight-hour timeline was performed to quantify fluxes under conditions identical to prior studies in 12-week old male GNMT-null mice and WT littermates [10]. Each stable isotope was purchased from Cambridge Isotope Laboratories, Inc (Tewksbury, MA, USA). Unless otherwise stated, all venous infusates were made with a 4.5% $^{2}H_2O$-enriched saline solution.

2.5. $^{2}H/^{13}C$ metabolic flux analysis

Derivatization of plasma glucose, gas chromatography-mass spectrometry analysis, and $^{2}H/^{13}C$ metabolic flux analysis were completed as previously outlined [10,26,27]. Briefly, mass isotopomer distributions were determined from fragment ion ranges: methyloxime pentapropionate derivatization of glucose, *m/z* 145—149; aldonitrile pentapropionate derivatization of glucose, *m/z* 173—178, 259—266, 284—291, and 370—379; di-*O*-isopropylidene propionate derivatization of glucose, *m/z* 301—314. For each sample, estimates of fluxes were repeated 50 times from random starting values. A chi-square test ($p = 0.05$) with 34 degrees of freedom was performed to determine goodness-of-fit. Flux estimates for each mouse are the average of values acquired from samples at 90, 100, and 110 min after initiating the [$^{13}C_3$]propionate bolus. The serial sampling confirmed isotopic steady state was achieved. The flux estimates were normalized to liver weight.

2.6. Blood and plasma analyses

Contour® blood glucose meters (Ascensia Diabetes Care, Parsippany, NJ, USA) were used to determine blood glucose concentration during stable isotope infusion studies. Non-esterified fatty acids were measured in plasma obtained at the 100-minute time point (seven hours and 40 min of fasting) from mice undergoing the stable isotope infusions via a colorimetric assay (NEFA C kit, Wako Chemicals USA Inc., Richmond, VA, USA). Arterial insulin was measured from plasma samples obtained at the 120-minute time point (eight hours of fasting) from mice receiving stable isotope infusions as previously performed [28].

2.7. Tissue collection and analyses

Eight-hour fasted, non-catheterized mice were sacrificed via cervical dislocation for analysis of liver metabolites, global DNA methylation, immunoblotting, and immunohistochemistry. Liver (tumor and non-tumor) was freeze-clamped within 20 s of sacrifice. Approximately 50 mg of liver tissue was sent to Human Metabolome Technologies America, Inc. (Boston, MA, USA) for targeted ionic metabolite quantification via capillary electrophoresis mass spectrometry (CE-TOFMS and CE-QqQMS) as previously described [29—32]. Hepatic triacylglycerides and glycogen were measured as previously outlined [33]. A DNeasy® Blood & Tissue Kit (Qiagen, Germantown, MD, USA) was used to isolate liver DNA and 5-methylcytosine (5-mC) was measured via an ELISA (EpiGentek Group Inc, Farmingdale, NY, USA, p-1030).

2.8. Immunoblotting

Liver tissue lysate was prepared as previously described [10,27]. At 70 or 95 °C, 20—40 μg of protein from liver homogenate samples were denatured and reduced. Liver proteins were separated using a NuPAGE 4—12% Bis-Tris gel (Invitrogen, Carlsbad, CA, USA) and, subsequently,

transferred to a PVDF membrane. PVDF membranes were probed with the following antibodies: acetyl-CoA carboxylase (ACC; 3662, Lot 4, 1:1000 dilution), DNA (cytosine-5)-methyltransferase 1 (DNMT1; 5032, Lot 1, 1:1000 dilution), glucose-6-phosphate dehydrogenase (G6PDH; 12263, Lot 1, 1:1000 dilution), fatty acid synthase (FASN; 3180, Lot 2, 1:1000), methylthioadenosine phosphorylase (MTAP; 4158, Lot 1, 1:1000 dilution), phospho-histone H2AX (γH2AX; 9718, Lot 13, 1:1000 dilution) and unconventional prefoldin RBP5 interactor (URI; 5844, Lot 1, 1:1000 dilution) from Cell Signaling Technology (Danvers, MA, USA); ATP-citrate lyase (ACLY; ThermoFisherScientific, Waltham, MA, USA, PA5-29495, dilution 1:1000); glutamate-cysteine ligase catalytic subunit (GCLC; ab207777, Lot GR284811-2, dilution 1:1000), glutamate-cysteine ligase modifier subunit (GCLM; ab153967, Lot GR113714-12, dilution 1:1000), glutathione synthetase (GSS; ab91591, Lot GR315302-4, dilution 1:1000), glycogen phosphorylase (PYGL; ab198268, Lot GR216725-18, 1:1000 dilution), poly(ADP-ribose) polymerase1 (PARP1; ab227244, Lot GR3226439-1, 1:1000 dilution) and pyruvate carboxylase (PC; ab126707, Lot GR95866-10, 1:1000 dilution) from Abcam (Cambridge, MA, USA); GNMT (Santa Cruz Biotechnology Inc., sc-68871, Lot K0712, dilution 1:1000); glutaryl-CoA dehydrogenase (GCDH; 14930-1-AP, 1:1000 dilution), nicotinamide N-methyltransferase (NNMT; 15123-1-AP, 1:1000 dilution) and tryptophan 2,3-dioxygenase (TDO; 15880-1-AP, 1:1000 dilution) from Proteintech® (Rosemont, IL, USA), and phosphatidylethanolamine methyltransferase (PEMT; Lifespan Bioscience Inc., Seattle, WA, USA, LS-C163519, Lot 53711, 1:1000 dilution). PVDF membranes were treated with a chemiluminescent HRP-substrate (MilliporeSigma, Billerica, MA, USA) following incubation with an HRP-conjugated secondary antibody. Imaging of membranes was completed using a ChemiDoc™ Imaging system and Image Lab™ software (Bio-Rad, Hercules, CA, USA). BLOT-FastStain (G-Bioscience, Geno Technology Inc., St. Louis, MO, USA) allowed total protein within a lane to be determined on the membrane and was used as a loading control. ImageJ software was utilized to obtain densitometry measurements.

2.9. Liver immunohistochemistry

Liver tissue was fixated using zinc formalin (ThermoFisherScientific, Waltham, MA, USA), paraffin-embedded, and sectioned (5 μm). Anti-Ki67 was used to assess cell proliferation. Anti-F4/80 was used to evaluate immune cell alterations in the liver. Immunohistochemistry was completed by the Vanderbilt Translational Pathology Shared Resource. Imaging was performed using whole slide digital images (20X magnification) which were acquired via a Leica SCN400 Slide Scanner (Leica Microsystems, Buffalo Grove, IL, USA). Leica SlidePath Digital Image Hub software (Leica Microsystems, Buffalo Grove, IL, USA) was employed to quantify immunostaining. Briefly, pixels of interest were manually selected to create a color definition file for each antibody. The parameters of the color definition file were applied to the entire section of tissue. For Ki67, two-to-three liver sections were analyzed per mouse to acquire the percent Ki67 positive nuclei using the measure stained cells algorithm. For F4/80, two-to-three liver sections per mouse were quantified. A measured stained area algorithm was used and the percent stained area was calculated as 100•(positive area•total tissue are^{-1}).

2.10. Real-time PCR

Liver RNA extraction, reverse transcription, real-time PCR were completed as previously described [27]. Real-time PCR was performed using albumin (Mm00802090_m1), α-fetoprotein (Mm00431715_m1), glyceraldehyde 3-phosphate dehydrogenase (GAPDH; Mm99999915_g1), and housekeeping gene, Rn18S (Mm03928990_g1), TaqMan™ gene expression assays (ThermoFisherScientific, Waltham, MA, USA).

2.11. Statistical analyses

A student's t-test or two-way repeated measures ANOVA were used to determine statistical differences ($p < 0.05$) followed by Bonferroni post hoc tests using SigmaStat® software (Systat Software Inc., San Jose, CA, USA). Data are reported as mean ± SEM.

3. RESULTS

3.1. GNMT KO mice exhibit hepatomegaly

In a large, ad libitum-fed cohort of mice, KO mice showed a ~6% decline in body weight due to decreased adiposity (Table 1). An eight hour fast alleviated this decrease in a separate cohort of KO mice (Table 1). The fasting-induced weight loss may mask the body weight differences between genotypes. We cannot rule out that the difference in body weight may require a larger cohort to identify the small reduction in adiposity in KO mice. KO mice displayed a ~2.25-fold increase in liver weight and liver-to-body weight (Table 1). Arterial insulin and non-esterified fatty acids were similar between genotypes during post-absorptive conditions (Table 1).

3.2. GNMT KO mice display liver methionine cycle dysregulation and tumorigenesis

GNMT, a regulator of methionine cycle and SAM homeostasis (Figure 1A), was undetectable in KO mice (Figure 1B). Methionine cycle intermediates, methionine, SAM, and SAH were increased in the livers of KO mice (Figure 1C). Sarcosine, a product of the reaction catalyzed by GNMT, was reduced in KO mice (Figure 1C). Metabolites associated with homocysteine remethylation to methionine were also altered.

Table 1 – Biometric characteristics in glycine N-methyltransferase-null mice. Body composition data are from 43-week-old, male glycine N-methyltransferase knockout (KO) mice and wildtype (WT) littermates with free access to food and water. Data are mean ± SEM for n = 16–19 mice per genotype. In a separate cohort of mice (Liver Characteristics), body weight, liver weight, and liver-to-body ratio were determined in WT and KO littermates following an 8-hour fast. Data are for mean ± SEM for n = 7–8 mice per genotype. Arterial plasma non-esterified fatty acids were obtained from catheterized WT and KO littermates undergoing stable isotope infusions 7 h and 40 min following food and water withdrawal. Data are mean ± SEM for n = 6–9 mice per genotype. Arterial plasma insulin was obtained from catheterized KO and WT littermates undergoing stable isotope infusions 8 h following food and water withdrawal. Data are mean ± SEM for n = 7–8 mice per genotype. For fasting studies, food and water were withdrawn during the first hour of the light cycle. Liver characteristics and plasma measurements were collected for male mice at 44 weeks of age.

Body Composition	WT	KO
Body Weight (g)	31.7 ± 0.5	29.9 ± 0.4*
Lean Mass (%)	69.4 ± 0.7	71.5 ± 0.4*
Fat Mass (%)	10.6 ± 0.7	8.5 ± 0.3*
Liver Characteristics		
Body Weight (g)	30.4 ± 0.9	30.5 ± 0.5
Liver Weight (g)	1.3 ± 0.0	2.9 ± 0.2*
Liver-to-Body Weight (%)	4.2 ± 0.1	9.5 ± 0.5*
Plasma Hormones and Metabolites		
Plasma Insulin (ng/ml)	0.48 ± 0.08	0.45 ± 0.11
Plasma Non-Esterified Fatty Acids (mmol/L)	0.72 ± 0.03	0.65 ± 0.06

*$p < 0.05$ vs WT.

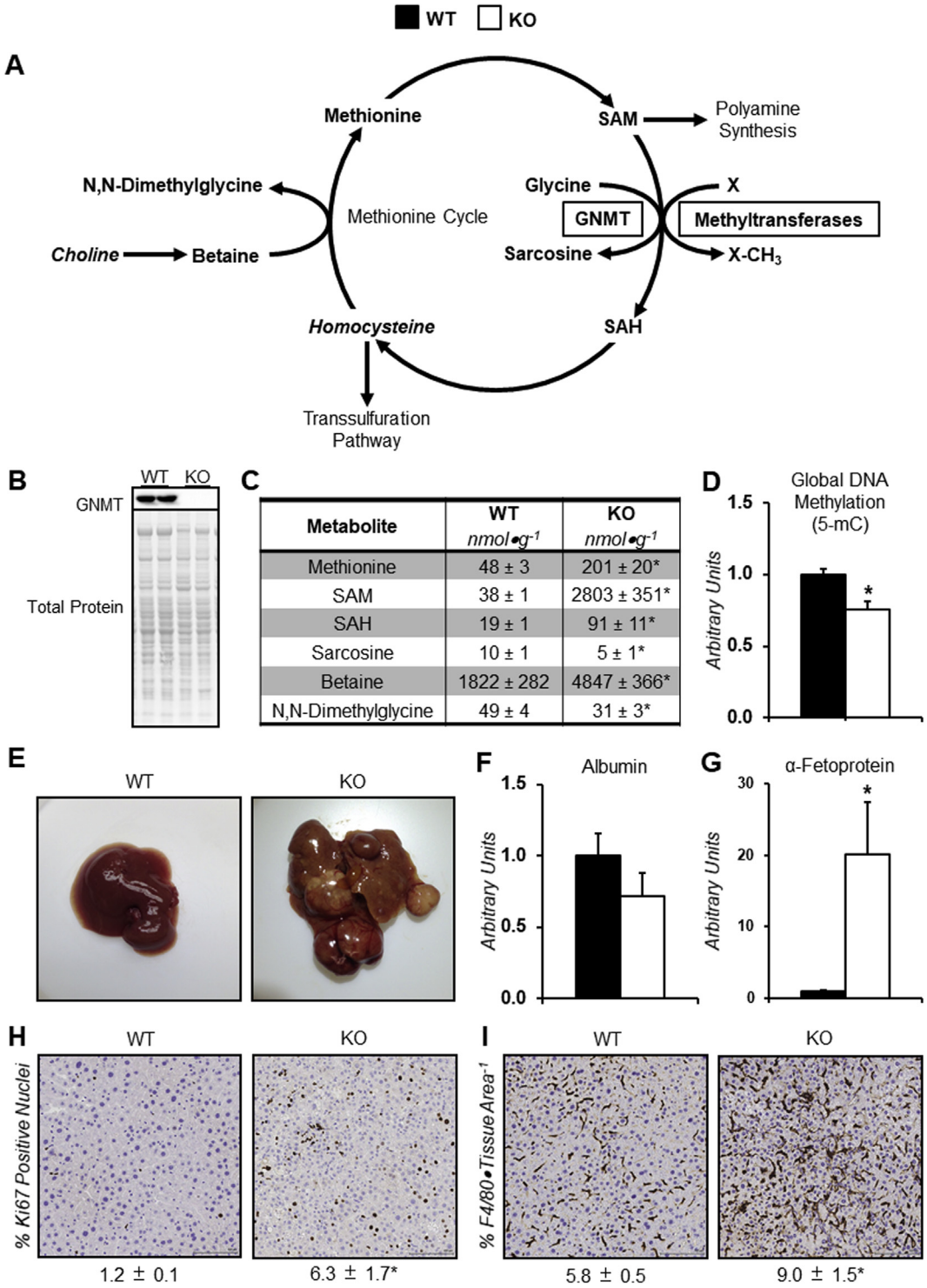

Figure 1: Methionine cycle dysregulation and pathological liver characteristics in glycine N-methyltransferase knockout mice. *A:* Schematic representation of select reactions, enzymes, and metabolites associated with one-carbon metabolism. Italicized metabolites were not measured. Enzymes are enclosed in boxes. *B:* Representative immunoblots of liver glycine N-methyltransferase (GNMT) from mice with a global deletion of GNMT (KO) and wildtype (WT) littermates. *C:* Liver metabolites related to the methionine cycle; methionine, S-adenosylmethionine (SAM), S-adenosylhomocysteine (SAH), sarcosine, betaine, and N, N-dimethylglycine (n = 8–9 per genotype). *D:* Liver 5-methylcytosine relative to total DNA (5-mC; n = 8–9 per genotype). *E:* Representative image of livers from WT and KO mice following an eight-hour fast. *F-G:* Liver albumin and α-fetoprotein mRNA (n = 9 per genotype). *H:* Percent Ki67 positive nuclei in livers with representative images (20X magnification; n = 8–9 per genotype). *I:* Percent F4/80 positive area per tissue area as determined by immunostaining with representative images (20X magnification; n = 8–9 per genotype). All data are from eight-hour fasted, male mice at 44 weeks of age. Data are mean ± SEM. *p < 0.05 vs. WT.

Specifically, betaine was increased and N, N-dimethylglycine was decreased in KO mice (Figure 1C). Liver global DNA methylation (5-mC) was reduced in KO mice (Figure 1D). The dysregulation of methionine cycle metabolism in KO mice was accompanied by liver nodules (Figure 1E). Liver albumin mRNA, a hepatocyte marker, was comparable between genotypes (Figure 1F). KO mice had a 20-fold increase in liver α-fetoprotein mRNA; an indicator of HCC (Figure 1G). Furthermore, GNMT KO mice showed increased liver cell proliferation as indicated by Ki67-positivie nuclei (Figure 1H). Livers of KO mice also showed increased immune cell infiltration as suggested by a higher proportion of F4/80 per tissue area (Figure 1I).

3.3. Reduced liver glucose production in GNMT KO mice

This study tested the hypothesis that HCC resulting from loss of GNMT-mediated transmethylation was associated with lower liver glucose formation and associated fluxes (Figure 2A). Reduced arterial blood glucose was observed throughout the majority of the experiment in KO mice (Figure 2B). This was linked to a lower endogenous glucose production in KO mice (V_{EndoRa}; Figure 2C). Glycogenolysis, the flux of glycogen to glucose-6-phosphate (V_{PYGL}), was diminished in KO mice (Figure 2C). Total gluconeogenic flux (V_{Aldo}) in KO mice was lower due to a decline in gluconeogenesis from phosphoenolpyruvate (V_{Enol}; Figure 2C). Despite a reduction in glycogenolysis and lower liver glycogen phosphorylase protein (Figure 2D) there were comparable liver glycogen levels between genotypes (Figure 2E). However, glycogen precursors, glucose-6 phosphate and UDP-glucose were lower in livers of KO mice (Figure 2G). GAPDH mRNA was higher in livers of KO mice (Figure 2F). In agreement with the decline in total gluconeogenesis, liver fructose-6-phosphate was reduced in KO mice (Figure 2G).

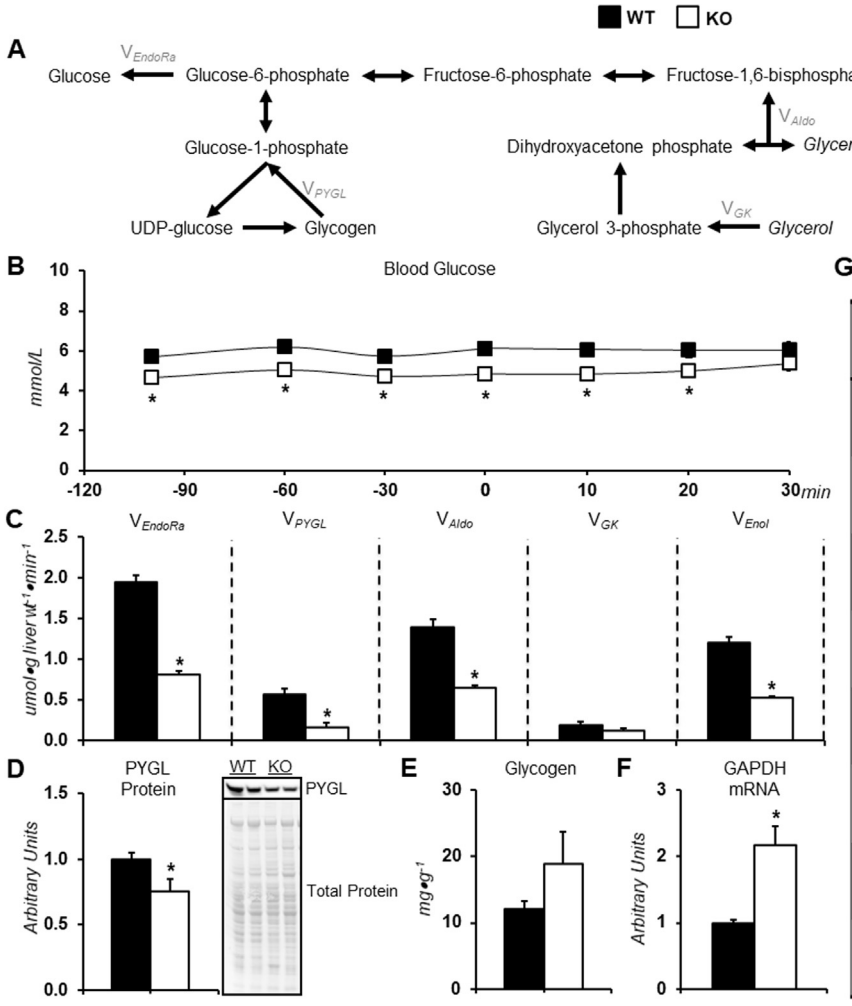

G

Metabolite	WT *nmol•g-1*	KO *nmol•g-1*
Glucose-6-phosphate	422 ± 28	214 ± 38*
Glucose-1-phosphate	35 ± 3	15 ± 4
UDP-glucose	560 ± 12	462 ± 28*
Fructose-6-phosphate	106 ± 11	68 ± 12*
Dihydroxyacetone phosphate	11 ± 6	6 ± 2
Glycerol-3-phosphate	291 ± 27	199 ± 34*
2-Phosphoglyceric acid	2.7 ± 0.4	1.9 ± 0.1
Phosphoenolpyruvic acid	7.6 ± 0.9	5.8 ± 0.5

Figure 2: Lower fluxes related to endogenous glucose production in glycine N-methyltransferase knockout mice. *A:* A schematic representation of select metabolites and fluxes (highlighted in gray) from $^{2}H/^{13}C$ metabolic flux analysis contributing to endogenous glucose production. *B:* A time course of fasting blood glucose concentration before, during, and after arterial sampling for $^{2}H/^{13}C$ metabolic flux analysis in wildtype (WT) and glycine N-methyltransferase knockout (KO) mice (n = 8–9 per genotype). *C:* Model-estimated, metabolic fluxes normalized to liver weight (μmol•g liver wt^{-1}•min^{-1}) in mice for endogenous glucose production (V_{EndoRa}), flux from glycogen to glucose-6-phosphate (V_{PYGL}), flux from dihydroxyacetone phosphate and glyceraldhyde-3-phosphate (V_{Aldo}), flux from glycerol to dihydroxyacetone phosphate (V_{GK}; hexose units), and flux from phosphoenolpyruvate to glyceraldehyde-3-phosphate (V_{Enol}; hexose units). n = 8–9 per genotype. *D:* Liver glycogen phosphorylase (PYGL) as determined by immunoblotting with a representative immunoblot (n = 7 per genotype). *E:* Liver glycogen concentration (mg•g liver wt^{-1}; n = 8–9 per genotype). *F:* Liver glyceraldehyde 3-phosphate dehydrogenase (GAPDH) mRNA (n = 9 per genotype). *G:* Metabolites related to glucose production; glucose-6-phosphate, glucose-1-phosphate, UDP-glucose, fructose-6-phosphate, dihydroxyacetone phosphate, glycerol-3-phosphate, 2-phosphoglyceric acid, and phosphoenolpyruvic acid (nmol•g liver wt^{-1}; n = 5–9 per genotype). All mice are males and 44 weeks of age. Data are mean ± SEM. *p < 0.05 vs. WT.

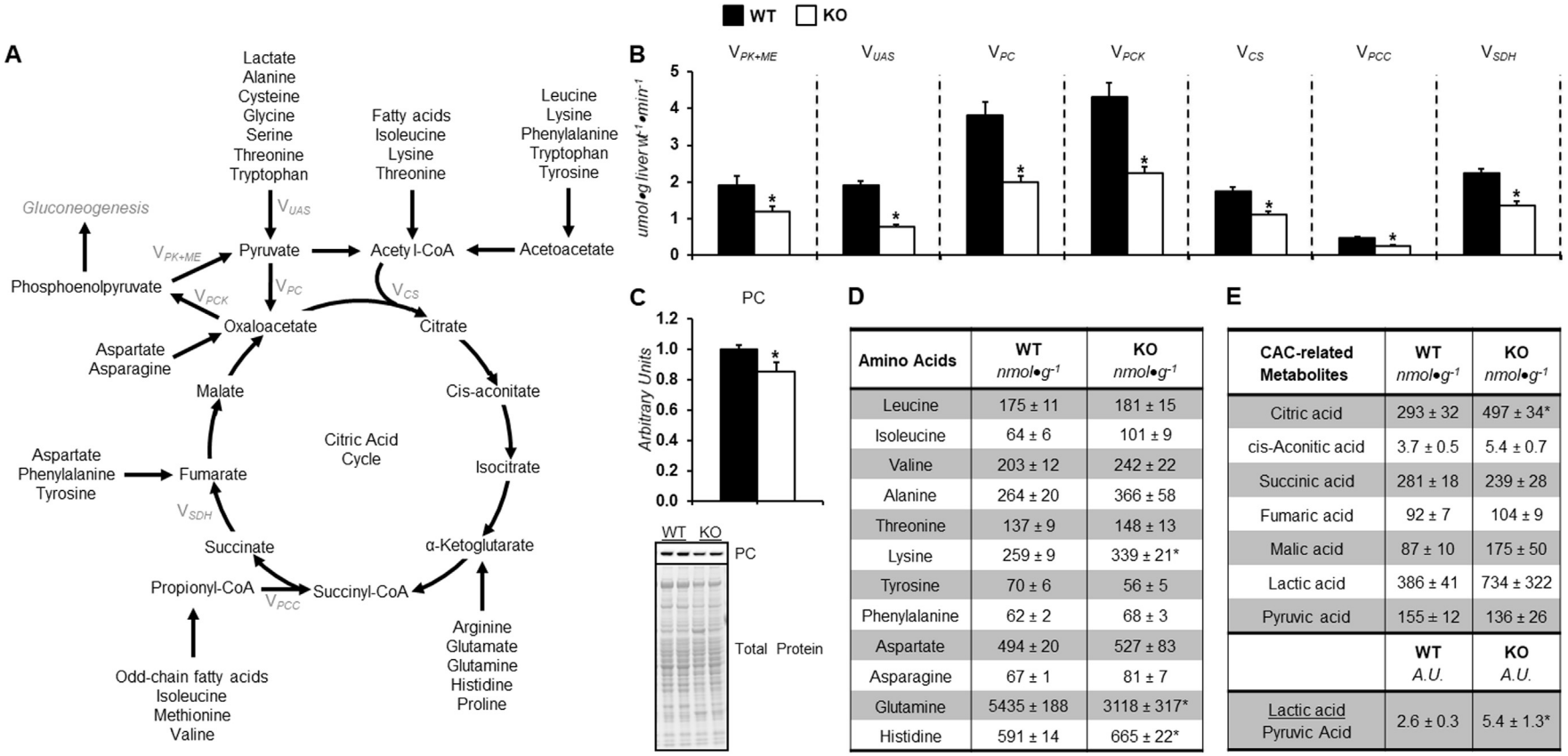

D

Amino Acids	WT *nmol•g^{-1}*	KO *nmol•g^{-1}*
Leucine	175 ± 11	181 ± 15
Isoleucine	64 ± 6	101 ± 9
Valine	203 ± 12	242 ± 22
Alanine	264 ± 20	366 ± 58
Threonine	137 ± 9	148 ± 13
Lysine	259 ± 9	339 ± 21*
Tyrosine	70 ± 6	56 ± 5
Phenylalanine	62 ± 2	68 ± 3
Aspartate	494 ± 20	527 ± 83
Asparagine	67 ± 1	81 ± 7
Glutamine	5435 ± 188	3118 ± 317*
Histidine	591 ± 14	665 ± 22*

E

CAC-related Metabolites	WT *nmol•g^{-1}*	KO *nmol•g^{-1}*
Citric acid	293 ± 32	497 ± 34*
cis-Aconitic acid	3.7 ± 0.5	5.4 ± 0.7
Succinic acid	281 ± 18	239 ± 28
Fumaric acid	92 ± 7	104 ± 9
Malic acid	87 ± 10	175 ± 50
Lactic acid	386 ± 41	734 ± 322
Pyruvic acid	155 ± 12	136 ± 26
	WT *A.U.*	KO *A.U.*
Lactic acid / Pyruvic Acid	2.6 ± 0.3	5.4 ± 1.3*

Figure 3: Diminished citric acid cycle-related fluxes in glycine N-methyltransferase knockout mice. *A:* A schematic representation of select metabolites and fluxes (highlighted in gray) from $^{2}H/^{13}C$ metabolic flux analysis associated with the citric acid cycle. *B:* Model-estimated, metabolic fluxes normalized to liver weight (μmol•g liver wt^{-1}•min^{-1}) in wildtype (WT) and glycine N-methyltransferase knockout (KO) mice for contribution of pyruvate kinase and malic enzyme to flux generating pyruvate (V_{PK+ME}), flux from non-phosphoenolpyruvate-derived, unlabeled anaplerotic substrate to pyruvate (V_{UAS}), anaplerotic flux as modeled by pyruvate to oxaloacetate (V_{PC}), cataplerosis modeled as oxaloacetate to phosphoenolpyruvate (V_{PCK}), flux from oxaloacetate and acetyl-CoA to citrate (V_{CS}), anaplerotic flux modeled as propionyl-CoA to succinyl-CoA (V_{PCC}), and flux from succinyl-CoA to oxaloacetate (V_{SDH}). n = 8–9 per genotype. *C:* Liver pyruvate carboxylase (PC) determined by immunoblotting and a representative immunoblot (n = 8 per genotype). *D:* Liver amino acids; leucine, isoleucine, valine, alanine, threonine, lysine, tyrosine, phenylalanine, aspartate, asparagine, glutamine, and histidine (nmol•g liver wt^{-1}; n = 8–9 per genotype). *E:* Liver citric acid cycle (CAC) and related metabolites; citric acid, cis-aconitic acid, succinic acid, fumaric acid, malic acid, lactic acid, pyruvic acid, and the lactic acid-to-pyruvic acid ratio (nmol•g liver wt^{-1}; n = 8–9 per genotype). All mice were males and 44-weeks-old. Data are mean ± SEM. *p < 0.05 vs. WT.

3.4. Lower citric acid cycle and associated fluxes in GNMT KO mice

The provision of gluconeogenic precursors is regulated by citric acid cycle (CAC) and related fluxes (Figure 3A). Flux of phosphoenolpyruvate to pyruvate (V_{PK+ME}), was lower in KO mice (Figure 3B). The rate of unlabeled, non-phosphoenolpyruvate derived, anaplerotic substrates to pyruvate (V_{UAS}; modeled as unlabeled lactate to pyruvate) was lower in KO mice (Figure 3B). Anaplerosis, modeled as flux from pyruvate to oxaloacetate (V_{PC}) and flux from propionyl-CoA to succinyl-CoA (V_{PCC}), were diminished in KO mice (Figure 3B). This was accompanied by a decline in pyruvate carboxylase (PC) protein (Figure 3C) and higher anaplerotic amino acids lysine and histidine (Figure 3D). Liver glutamine was lower in KO mice, suggesting that, despite reduced anaplerosis related to glucose production, glutaminolysis may be increased in KO mice (Figure 3D). KO mice displayed a reduction in cataplerotic flux (V_{PCK}), modeled as metabolite flux from oxaloacetate to phosphoenolpyruvate (Figure 3B). A decline in CAC fluxes (V_{CS} and V_{SDH}) was also exhibited by KO mice (Figure 3B). This was associated with an increase in liver citric acid concentration (Figure 3E). Of note, while lactic acid and pyruvic acid were comparable between genotypes, the lactic acid-to-pyruvic acid ratio was increased in the livers of KO mice (Figure 3E).

3.5. Dysregulated NAD^+ metabolism in livers of GNMT KO mice

The increased lactic acid-to-pyruvic acid ratio indicates dysregulated redox state in the livers of KO mice. Indeed, liver NAD^+, NADH, and the NAD^+-to-NADH ratio was reduced in KO mice (Figure 4B–D). Alterations at multiple metabolic nodes of NAD^+ regulation may be involved in the perturbed NAD^+ homeostasis (Figure 4A). In the absence of GNMT, there is an increase in the protein of other methyltransferases including DNMT1 (Supp Fig. A.1A), PEMT (Supp Fig. A.1B) and, most notably for NAD^+ regulation, NNMT (Figure 4E). This increase constrains the elevated SAM at the expense of NAD^+ salvage. NAD^+ is an important substrate involved in the DNA damage response. Livers of GNMT KO mice displayed increased γH2AX (Figure 4F), higher PARP1 protein (Figure 4G), and lower ADP-ribose (Figure 4H). These markers indicate utilization of NAD^+ in response to DNA damage is elevated. Also, de novo synthesis of NAD^+ may be impaired as tryptophan was higher (Figure 4I), TDO protein was lower (Figure 4J), and negative regulator of TDO expression, URI, was higher (Figure 4K) in KO mice. It

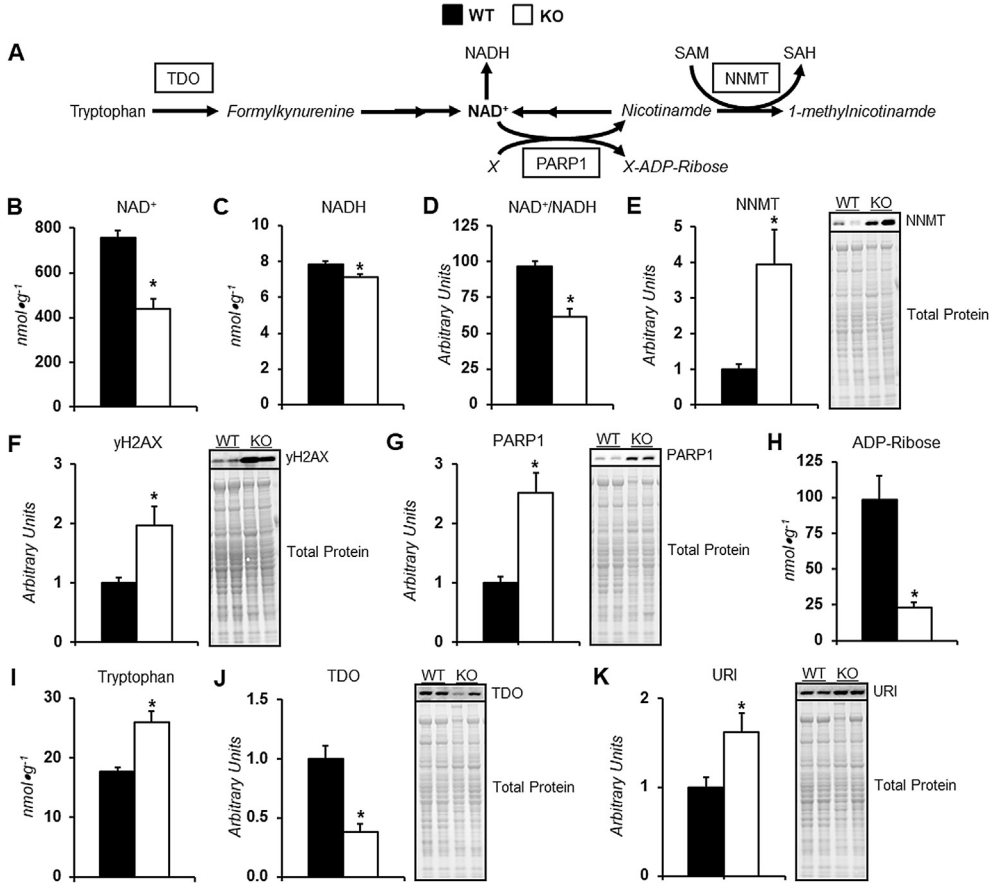

Figure 4: Dysregulated NAD^+ homeostasis in livers of glycine N-methyltransferase knockout mice. *A:* A schematic representation of select metabolites and enzymes associated with NAD^+ synthesis, salvage, and utilization. *B-D:* Liver metabolites related to redox state in wildtype (WT) and glycine N-methyltransferase deficient (KO) mice; NAD^+, NADH, and the NAD^+-to-NADH ratio (nmol•g liver wt^{-1}; n = 8–9 per genotype). *E:* Liver nicotinamide N-methyltransferase (NNMT) as determined by immunoblotting with a representative immunoblot (n = 7 per genotype). *F:* Liver phosphorylated histone H2AX variant (γH2AX) as determined by immunoblotting with a representative immunoblot (n = 7–8 per genotype). *G:* Liver poly(ADP-ribose) polymerase 1 (PARP1) as determined by immunoblotting with a representative immunoblot (n = 8 per genotype). *H:* Liver ADP-ribose (nmol•g liver wt^{-1}; n = 9 per genotype). *I:* Liver tryptophan (nmol•g liver wt^{-1}; n = 8–9 per genotype). *J:* Liver tryptophan 2,3-dioxygenase (TDO) as determined by immunoblotting with a representative immunoblot (n = 7 per genotype). *K:* Liver unconventional prefoldin RPB5 interactor (URI) as determined by immunoblotting with a representative immunoblot (n = 6–7 per genotype). All data are from eight-hour fasted, male mice at 44 weeks of age. Data are mean ± SEM. *p < 0.05 vs. WT.

is important to note that a potential impairment in NAD^+ salvage due to increased NNMT occurs prior to tumorigenesis in GNMT KO mice (Supp Fig. A.2A). However, increased NAD^+ utilization and reduced de novo synthesis of NAD^+ coincide with tumorigenesis given that γH2AX (Supp Fig. A.2B), PARP1 (Supp Fig. A.2C), TDO (Supp Fig. A.2D), and URI (Supp Fig. A.2E) are comparable between genotypes at 12 weeks of age, prior to the appearance of HCC in GNMT KO mice.

3.6. Altered pentose phosphate pathway metabolism in GNMT KO mice

While reduced NAD^+ availability impedes CAC fluxes and, consequently, gluconeogenesis, it may also perturb redox status so that precursors of glucose production are directed towards other pathways such as the pentose phosphate pathway to preserve reducing equivalent availability (Figure 5A). KO mice exhibited an increase in G6PDH protein (Figure 5B). Liver $NADP^+$ was reduced in KO mice (Figure 5C). NADPH was comparable between genotypes (Figure 5D); however, the $NADP^+$-to-NADPH ratio was lowered in KO mice (Figure 5E). Liver 6-phosphogluconic acid was diminished in KO mice (Figure 5F). Ribulose-5-phosphate (R5P) was elevated (Figure 5G) and the G6P-to-R5P ratio (Figure 5H) was reduced in KO mice. Together, these data provide support for increased flux through the oxidative phase of the pentose phosphate pathway in the absence of GNMT.

3.7. Elevated transsulfuration and glutathione (GSH) synthesis in KO mice

NADPH is an important reducing equivalent for maintaining GSH levels. In livers of KO mice where NADPH availability may be challenged, the elevated SAM may promote the de novo synthesis of GSH via higher transsulfuration (Figure 6A). Transsulfuration-related metabolites are altered in livers of KO mice. Serine is reduced (Figure 6B), cystathionine is increased (Figure 6C), and cysteine trends towards being elevated (Figure 6D) in KO mice. Also, KO mice showed a decline in glycine (Figure 6F) and increase in GSH (Figure 6G). The elevated GSH was associated with increased glutathione synthetase protein (Figure 6K). Importantly, GSH synthesis utilizes gluconeogenic precursors and may contribute to the decline in glucose formation.

3.8. Liver steatosis is absent in GNMT KO mice at 44 weeks of age

The altered redox state has implications for metabolic systems beyond glucose production, including lipogenesis. URI target, glutaryl-CoA dehydrogenase (GCDH), was reduced in KO mice (Supp Fig. A.3A). This may contribute to the lower acetyl-CoA concentration in KO mice (Supp Fig. A.3B). GNMT-deficient mice exhibit elevated liver malonyl-CoA and triacylglycerides prior to the appearance of HCC at 12 weeks of age [10]. However, at 44 weeks of age, when liver tumor nodules are present, malonyl-CoA and triacylglycerides are comparable between genotypes (Supp Figure A.3C and D). Of note, the normalization of liver steatosis in 44-week-old KO mice may also be the result of lower de novo lipogenesis given ATP-citrate lyase and fatty acid synthase are reduced (Supp Figure A.3E and G). A persistent elevation in polyamine turnover from 12- to 44 weeks of age may also limit triglyceride accumulation by using acetyl-CoA for polyamine catabolism (Supp Fig. A.4).

4. DISCUSSION

Studies in humans and mutant mouse models highlight a role for GNMT insufficiency in the pathogenesis of HCC [16–19]. Our previous work identified that liver glucose production from multiple sources was

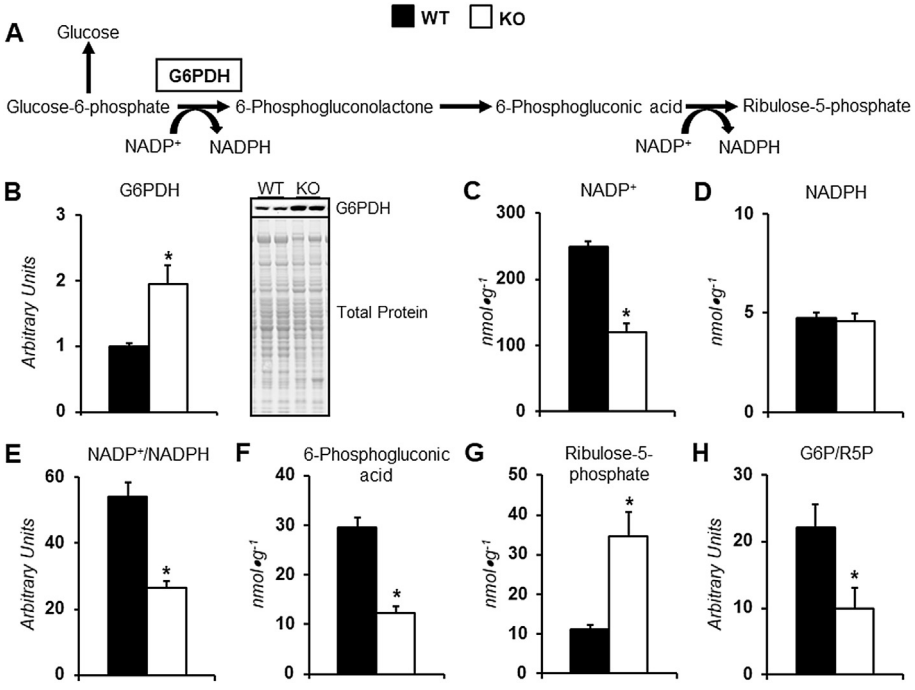

Figure 5: Alterations in the pentose phosphate pathway of glycine N-methyltransferase knockout mouse livers. *A:* A schematic representation of select enzymes and metabolites related to the pentose phosphate pathway. *B:* Liver glucose-6-phosphate dehydrogenase (G6PDH) in wildtype (WT) and glycine N-methyltransferase knockout (KO) mice as determined by immunoblotting with a representative immunoblot (n = 7–8 per genotype). *C-H:* Liver metabolites related to the pentose phosphate pathway; $NADP^+$, NADPH, the $NADP^+$-to-NADPH ratio, 6-phosphogluconic acid, ribulose 5-phosphate (R5P), and the glucose-6-phosphate (G6P)-to-R5P ratio (nmol•g liver wt^{-1} or arbitrary units as indicated; n = 8–9 per genotype). All data are from eight-hour fasted, male mice at 44 weeks of age. Data are mean ± SEM. *p < 0.05 vs. WT.

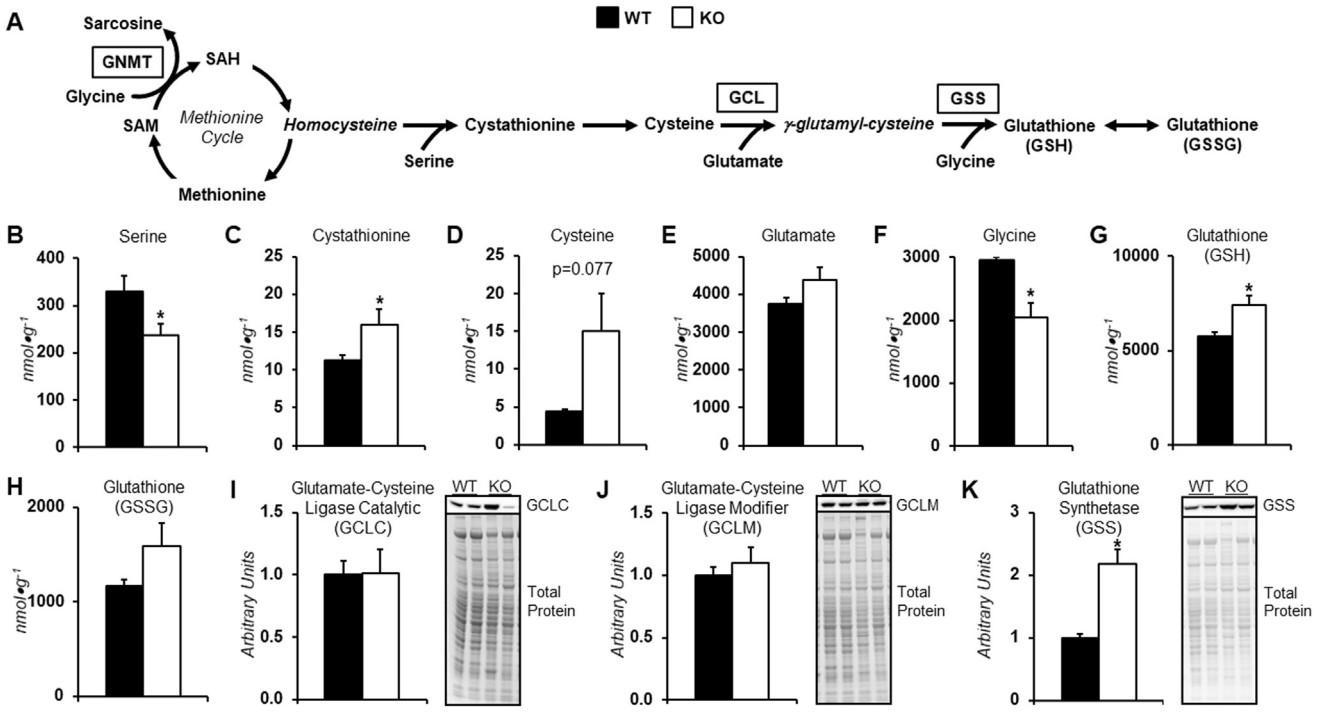

Figure 6: Increased liver glutathione in glycine N-methyltransferase knockout mice. *A:* A schematic representation of select metabolites and reactions related to de novo glutathione synthesis. *B-H:* Liver metabolites related to de novo glutathione synthesis (nmol•g liver wt^{-1}; n = 6–9 per genotype) in wildtype (WT) and glycine N-methyltransferase-deficient (KO) mice; serine, cystathionine, cysteine, glutamate, glycine, reduced glutathione (GSH), and oxidized glutathione (GSSG). *I:* Liver glutamate-cysteine ligase catalytic subunit (GCLC) as determined by immunoblotting with a representative immunoblot (n = 7–8 per genotype). *J:* Liver glutamate-cysteine ligase modifier subunit (GCLM) as determined by immunoblotting with a representative immunoblot (n = 7–8 per genotype). *K:* Liver glutathione synthetase (GSS) as determined by immunoblotting with a representative immunoblot (n = 7 per genotype). All data are from eight-hour fasted, male mice at 44 weeks of age. Data are mean ± SEM. *p < 0.05 vs. WT.

impaired in 12-week-old GNMT-null mice prior to the appearance of HCC [10]. A reduction in liver glucose production has been theorized not only to mediate the development of liver tumorigenesis but also to sustain it by sparing biosynthetic nutrients and energy resources for tumorigenic processes [9–11,34]. For example, mice lacking liver glucose-6-phosphatase (G6PC) display reduced fasting glucose formation that is associated with a subsequent development of hepatic tumors with age [35–37]. Furthermore, a shunting of G6P to the pentose phosphate pathway and enhanced use in glycolysis has been linked to the tumorigenic phenotype [35]. The present studies extend earlier studies conducted prior to HCC by measuring changes in liver glucose production and associated fluxes in the conscious, unrestrained 44-week-old GNMT KO mouse with HCC. It was hypothesized that impaired glucose formation in GNMT-null mice would persist in the presence of HCC. $^{2}H/^{13}C$ MFA showed glucose production from glycogen and gluconeogenic sources was reduced in the KO mice with liver tumors. The estimates of nutrient flux were supported by results of metabolomic and molecular analyses that support the conclusion that livers of KO mice redirect glucose precursors to pathways that regulate redox state (i.e. the pentose phosphate pathway and de novo synthesis of GSH). Furthermore, these changes in nutrient handling are coupled to lower liver NAD^{+} availability. The results shown here in GNMT KO mice extend our previous work by showing that the reduction in glucose formation in 12-week-old GNMT KO mice prior to the appearance of HCC is sustained through the manifestation of HCC. Moreover, results show livers of KO mice at 44 weeks of age display a more pronounced dysregulation of NAD^{+} homeostasis compared to 12-week-old mice (See Supp Table A.1 for a summary of metabolic characteristics in 12- and 44-week old KO mice). It is proposed that liver glucose control and redox state are key components of the metabolic program that underlies the pathogenesis of HCC in KO mice (Figure 7).

4.1. Glucose formation in the livers of KO mice

Blood glucose was reduced in postabsorptive KO mice with HCC. This adds to prior work in GNMT-null mice studied before the appearance of HCC [10,38,39]. Here we show the lower blood glucose concentration was due to a decrease in endogenous glucose production (V_{EndoRa}). The decline in glucose formation is, in part, the result of a lower contribution of glycogen to glucose synthesis (V_{PYGL}). Impaired glycogenolysis and increased glycogen have been reported in GNMT-deficient mice at time points prior to liver tumor formation [10,39,40]. The present study showed that this is due in part to lower liver glycogen phosphorylase. Liver glycogen was not significantly elevated in 44-week-old KO mice as previously reported in 11–12-week old GNMT-deficient mice. This may be due to a limitation in glycogen precursors, glucose-6-phosphate and UDP-glucose, which were lower in KO mice. Additionally, the impaired glycogenolysis and the absence of elevated glycogen could be linked to increased use of glucose-6-phosphate in the pentose phosphate pathway (detailed below).

Concurrent with a reduction in glycogenolysis, was a decline in gluconeogenic flux from phosphoenolpyruvate (V_{Enol}) and total gluconeogenesis (V_{Aldo}) in KO mice. The aforementioned impairments could mediate the lower liver fructose-6-phosphate in KO mice. The limitation in fructose-6-phosphate for glucose formation may be a common feature of HCC as a reduction in fructose-1,6-biphosphatase has been reported [11,34,41–43]. Gluconeogenesis is also governed by

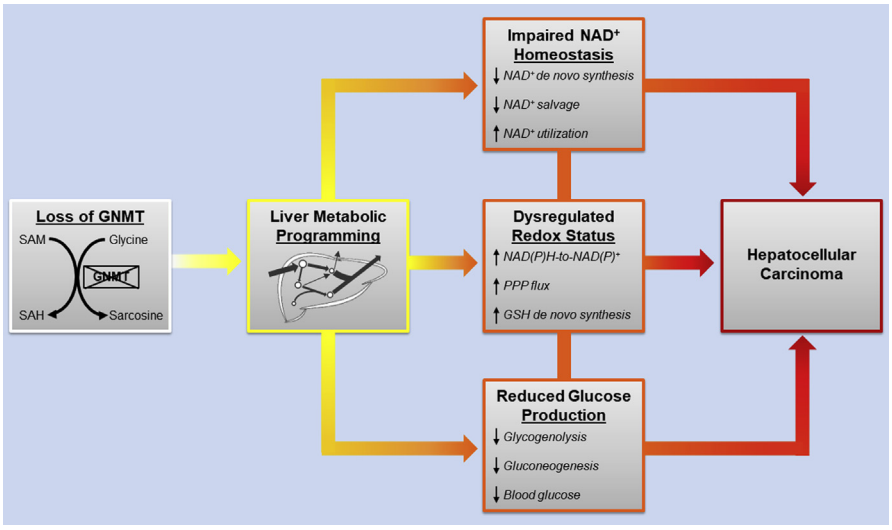

Figure 7: Schematic representation of hypothesized metabolic programming contributing to the development of HCC in livers of GNMT KO mice.

anaplerosis, cataplerosis, and CAC-related fluxes. Total cataplerosis (V_{PCK}) and anaplerotic fluxes (V_{PCC} and V_{PC}) were reduced in KO mice. Regulators of anaplerosis including a reduction in CAC fluxes (V_{SDH} and V_{CS}), PC protein, and unlabeled anaplerotic substrate flux to pyruvate (V_{UAS}) may mediate the slowing of metabolite entry into the CAC.

The metabolic fluxes were estimated from the mass isotopomer distribution of circulating glucose and normalized to liver weight; which is ~2.25-fold greater in GNMT KO mice. Given this, the conclusion that glucose formation and associated nutrient fluxes are reduced in GNMT KO mice assumes that the proportion of liver weight that is made up of hepatocytes is comparable between genotypes and that these cells produce glucose. Albumin mRNA, a hepatocyte marker, was comparable in livers of KO mice. It is important to consider that KO mice showed ~20-fold higher liver α-fetoprotein mRNA. Alpha-fetoprotein is expressed in hepatocyte precursor cells such as oval cells [44,45]. In fact, increased proliferation of oval cells contributes to tumor formation and the pathogenesis of HCC in GNMT-null mice [15,46]. Thus, it is reasonable to conclude that a similar or greater proportion of hepatocyte lineage cells are present in livers of KO mice. These cells, however, exhibit more heterogeneity in hepatocyte maturation.

4.2. Redox state in livers of KO mice

Glucose production and associated intermediary metabolic fluxes are closely linked to redox potential. Elevated cytosolic NADH and/or NADH/NAD^+ are inhibitory for gluconeogenesis from lactate [22,23]. Moreover, NAD^+ is a required cofactor in CAC reactions and the downstream generation of ATP required for gluconeogenesis. KO mice showed a decline in liver NAD^+, NADH, and the NAD^+-to-NADH ratio. These changes in redox parameters may impede gluconeogenesis in KO mice. The measured NAD^+-to-NADH does not distinguish between cell compartmentation. However, the lactate-to-pyruvate ratio is an indicator of the cytosolic NADH-to-NAD^+ ratio [47]. In GNMT KO mice, liver lactic acid relative to pyruvic acid was higher. Interestingly, the reduction in NAD^+ was more substantial than NADH. Metabolic processes independent of gluconeogenesis could prevent a similar decline in oxidized and reduced NAD^+. For example, the mRNA of the glycolytic enzyme, GAPDH, was elevated in GNMT KO mice. An increase in GAPDH action and/or glycolysis may impede the decline in NADH relative to NAD^+. Alternatively, we have previously shown respiration to be impaired in hepatocytes from 12-week-old GNMT KO mice [10]. A reduction in oxidative phosphorylation could blunt the lowering of liver NADH in GNMT KO mice at 44 weeks of age.

The redox phenotype in KO mice is linked to the dysregulation of pathways associated with NAD^+ provision and utilization. Lower liver NAD^+ and its precursor, nicotinamide (NAM), are observed in KO mice as early as 12 weeks of age [10]. Here we show NNMT protein to be elevated in livers of KO mice prior to HCC at 12 weeks of age and in 44-week old mice when HCC is present. NNMT transfers a methyl group from SAM to NAM forming 1-methylnicotinamide and SAH [48]. The increase in NNMT has been proposed to be a compensatory mechanism to prevent elevated liver SAM [10,21]. Indeed, liver SAM is reduced in GNMT-deficient mice when NNMT substrate, NAM, is not limiting [21]. However, overexpression of NNMT does not lower liver SAM in WT mice [49]. Thus, the ability of NNMT to control liver methyl donor balance is of importance only under conditions where it is positioned to be a predominant methyltransferase such as is the case in mice with GNMT-deficient livers [49]. There is limited evidence to suggest that NNMT is a primary regulator of liver NAM homeostasis. Antisense and adenoviral knockdown of NNMT did not increase liver NAM and NAD^+ in mice [50,51]. However, NNMT-null mice display an increase in plasma NAM under high-fat fed conditions [52]. It is important to note that high-fat feeding lowers liver GNMT levels [53]. Thus, it is hypothesized that the elevated NNMT lowers NAM and, subsequently, compromises NAD^+ salvage under conditions of GNMT insufficiency. Intriguingly, supplementing the drinking water of GNMT-null mice with NAM prevents liver steatosis that precedes HCC in this mouse model [21]. Enhancing NAD^+ provision may also inhibit HCC GNMT-null mice.

In addition to salvage processes, NAD^+ is synthesized de novo from tryptophan via the kynurenine pathway [54]. De novo synthesis of NAD^+ is primarily localized to the liver *in vivo* [55]. Here we show livers of KO mice exhibited an increase in tryptophan and a reduction in TDO, the hepatic enzyme catalyzing the conversion of tryptophan to N′-formylkynurenine [56]. This strongly implies that reduced NAD^+ synthesis via the kynurenine pathway may be facilitated by the increase in liver URI observed in KO mice. Mouse models overexpressing and insufficient in URI show a reduction and increase in liver NAD^+, respectively [57]. Evidence suggests that URI reduces NAD^+ by

inhibiting aryl hydrocarbon receptor- and/or estrogen receptor-mediated expression of kynurenine pathway regulators such as TDO [57]. The URI gain-of-function in mice also invokes liver DNA damage and tumorigenesis that is prevented by supplementing the mouse diet with NAD^+ precursor nicotinamide riboside [57]. An increase in liver URI may hold translational implications. URI is increased in humans with HCC and the magnitude of the increase in expression is associated with poor survival [57]. Beyond the kynurenine pathway, the higher URI potentially impacts liver lipid synthesis. At 12 weeks of age, GNMT-deficient mice are characterized by liver triacylglyceride accumulation and higher levels of enzymes involved in de novo lipogenesis [10]. Interestingly, here we show 44-week old KO mice no longer display liver steatosis. This is associated with a reduction in the protein of enzymes involved in de novo lipogenesis. It is notable that these enzymes are lower in livers of URI-overexpressing mice [57,58].

Results indicate that diminished liver NAD^+ is the product of accelerated NAD^+-consuming enzymes, including PARPs. PARPs transfers ADP-ribose from NAD^+ to acceptor proteins to form ADP-ribose polymers [59]. PARP action is a substantial contributor to NAD^+ catabolism in the cell [55,60]. In the liver, pharmacological inhibition of PARP elevates NAD^+ [61,62]. PARP-mediated poly(ADP-ribosyl)ation are involved in the control of many processes including the DNA damage response [59]. The NAD^+-consuming action of PARPs is profound in response to genotoxic stresses that damage DNA [55,63–65]. This is owing to the increase in PARP catalytic activity upon binding to DNA strand breaks [60,66]. Liver PARP1 was higher in livers of 44- but not 12-week old KO mice. This is accompanied by an increase in DNA damage response marker, γH2AX. Thus, the lower NAD^+ in KO mice with HCC may be related to genomic insult.

4.3. Diversion of glucose precursors towards pathways regulating redox potential in KO mice

An alternative fate to glucose production for glucose-6-phosphate is the oxidative phase of the pentose phosphate pathway [67]. The oxidative pentose phosphate pathway is an important source of intracellular NAPDH for reductive biosynthetic reactions and redox homeostasis [68,69]. Liver $NADP^+$ and NADPH were lower and unchanged, respectively, in KO mice. This created a lower $NADP^+$-to-NADPH ratio which was associated with an increase in liver G6PDH protein. G6PDH is a key controller of flux through the oxidative pentose phosphate pathway and is routinely observed to be higher in HCC models with elevated pentose phosphate pathway flux [70]. Furthermore, livers of KO mice showed a decrease in the G6P-to-R5P ratio; an indicator of increased flux through the pentose phosphate pathway [71]. Generating reducing potential via the pentose phosphate pathway to mitigate oxidative stress is protective for many cancer types [67]. The enhanced need for antioxidant defense may accelerate flux through the pentose phosphate pathway in the liver of this mouse model.

While NADPH is a cofactor in the reduction of GSSG to GSH, GSH is also generated de novo via two reactions catalyzed by glutamate-cysteine ligase and GSS [72,73]. Liver glutamate-cysteine ligase subunits (GCLC and GCLM) and reactants (glutamate and cysteine) were similar between genotypes. The increase in cysteine did not reach statistical significance, however, cystathionine was higher and serine was lower in KO mice. This suggests increased flux and cysteine provision through the transsulfuration pathway in response to elevated SAM. GSS protein and GSH in the livers of KO mice were higher. Results indicate increased de novo synthesis of GSH downstream of higher transsulfuration in the livers of KO mice. A greater formation of GSH diverts gluconeogenic precursors (cysteine and glutamate) away from glucose formation in KO mice. Given the positive association between GSH and cell proliferation [73], it is reasonable to further hypothesize that the increased GSH promotes HCC in KO mice.

5. CONCLUSION

Metabolic reprogramming supports tumor formation. As such, metabolic nodes and pathways that are pivotal to this reprogramming may be effectively targeted for cancer therapeutics. GNMT KO mice with HCC exhibit a reduction in glucose formation from glycogen and gluconeogenic sources. Precursors for glucose are diverted to alternative biosynthetic pathways that can contribute to tumorigenesis. These include the pentose phosphate pathway and de novo GSH synthesis. The shift in metabolic fluxes are associated with a reduction in NAD^+ and the NAD^+-to-NADH ratio. The perturbation in NAD^+ may be a product of a blockade in the kynurenine pathway, competition for NAM, and/or consumption of NAD^+. It can be concluded from these studies that accelerating glucose formation directly and/or indirectly via NAD^+ homeostasis holds potential to combat HCC in GNMT-null mice.

AUTHOR CONTRIBUTIONS

CCH and DHW designed the experiments. CCH, FDJ, ZW, and MG contributed to data acquisition. CCH analyzed and interpreted data. CCH drafted the manuscript. All authors contributed to editing the manuscript and approved the manuscript for publication.

CONFLICT OF INTEREST

No conflicts of interest, financial or otherwise, are declared by the authors.

ACKNOWLEDGEMENTS

The authors acknowledge the technical expertise of the Mouse Metabolic Phenotyping Center Analytical Core Services at Vanderbilt University. The Vanderbilt University Medical Center Digital Histology Shared Resource completed the whole slide imaging. This research was supported by the National Institute of Diabetes and Digestive and Kidney Diseases Grants DK050277 and DK054902 (DHW) and Diabetes Canada Postdoctoral Fellowship (CCH). The Mouse Metabolic Phenotyping Center Analytical Core Services are supported by National Institute of Diabetes and Digestive and Kidney Diseases Grants DK059637 and DK020593.

APPENDIX A. SUPPLEMENTARY DATA

Supplementary data to this article can be found online at https://doi.org/10.1016/j.molmet.2019.02.006.

REFERENCES

[1] Jemal, A., Ward, E.M., Johnson, C.J., Cronin, K.A., Ma, J., Ryerson, B., et al., 2017. Annual report to the nation on the status of cancer, 1975-2014, Featuring Survival. Journal of the National Cancer Institute 109.

[2] Islami, F., Miller, K.D., Siegel, R.L., Fedewa, S.A., Ward, E.M., Jemal, A., 2017. Disparities in liver cancer occurrence in the United States by race/ethnicity and state. CA: A Cancer Journal for Clinicians 67:273–289.

[3] Bray, F., Ferlay, J., Soerjomataram, I., Siegel, R.L., Torre, L.A., Jemal, A., 2018. Global cancer statistics 2018: GLOBOCAN estimates of incidence and mortality worldwide for 36 cancers in 185 countries. CA: A Cancer Journal for Clinicians 68:394–424.

[4] DeBerardinis, R.J., Chandel, N.S., 2016. Fundamentals of cancer metabolism. Science Advances 2:e1600200.
[5] Pavlova, N.N., Thompson, C.B., 2016. The Emerging Hallmarks of Cancer Metabolism. Cell Metabolism 23:27–47.
[6] Shi, H., Fang, R., Li, Y., Li, L., Zhang, W., Wang, H., et al., 2016. The oncoprotein HBXIP suppresses gluconeogenesis through modulating PCK1 to enhance the growth of hepatoma cells. Cancer Letters 382:147–156.
[7] Wang, B., Hsu, S.H., Frankel, W., Ghoshal, K., Jacob, S.T., 2012. Stat3-mediated activation of microRNA-23a suppresses gluconeogenesis in hepatocellular carcinoma by down-regulating glucose-6-phosphatase and peroxisome proliferator-activated receptor gamma, coactivator 1 alpha. Hepatology 56:186–197.
[8] Bian, X.L., Chen, H.Z., Yang, P.B., Li, Y.P., Zhang, F.N., Zhang, J.Y., et al., 2017. Nur77 suppresses hepatocellular carcinoma via switching glucose metabolism toward gluconeogenesis through attenuating phosphoenolpyruvate carboxykinase sumoylation. Nature Communications 8:14420.
[9] Ma, R., Zhang, W., Tang, K., Zhang, H., Zhang, Y., Li, D., et al., 2013. Switch of glycolysis to gluconeogenesis by dexamethasone for treatment of hepatocarcinoma. Nature Communications 4:2508.
[10] Hughey, C.C., Trefts, E., Bracy, D.P., James, F.D., Donahue, E.P., Wasserman, D.H., 2018. Glycine N-methyltransferase deletion in mice diverts carbon flux from gluconeogenesis to pathways that utilize excess methionine cycle intermediates. Journal of Biological Chemistry 293:11944–11954.
[11] Chen, M., Zhang, J., Li, N., Qian, Z., Zhu, M., Li, Q., et al., 2011. Promoter hypermethylation mediated downregulation of FBP1 in human hepatocellular carcinoma and colon cancer. PLoS One 6:e25564.
[12] McFadzean, A.J., Yeung, R.T., 1969. Further observations on hypoglycaemia in hepatocellular carcinoma. Americas Journal of Medicine 47:220–235.
[13] Yeung, R.T., 1997. Hypoglycaemia in hepatocellular carcinoma: a review. Hong Kong Medical Journal 3:297–301.
[14] Tsai, C.Y., Chou, S.C., Liu, H.T., Lin, J.D., Lin, Y.C., 2014. Persistent hypoglycemia as an early, atypical presentation of hepatocellular carcinoma: a case report and systematic review of the literature. Oncology Letters 8:1810–1814.
[15] Lu, S.C., Mato, J.M., 2012. S-adenosylmethionine in liver health, injury, and cancer. Physiological Reviews 92:1515–1542.
[16] Avila, M.A., Berasain, C., Torres, L., Martin-Duce, A., Corrales, F.J., Yang, H., et al., 2000. Reduced mRNA abundance of the main enzymes involved in methionine metabolism in human liver cirrhosis and hepatocellular carcinoma. Journal of Hepatology 33:907–914.
[17] Chen, Y.M., Shiu, J.Y., Tzeng, S.J., Shih, L.S., Chen, Y.J., Lui, W.Y., et al., 1998. Characterization of glycine-N-methyltransferase-gene expression in human hepatocellular carcinoma. International Journal of Cancer 75:787–793.
[18] Martinez-Chantar, M.L., Vazquez-Chantada, M., Ariz, U., Martinez, N., Varela, M., Luka, Z., et al., 2008. Loss of the glycine N-methyltransferase gene leads to steatosis and hepatocellular carcinoma in mice. Hepatology 47:1191–1199.
[19] Liao, Y.J., Liu, S.P., Lee, C.M., Yen, C.H., Chuang, P.C., Chen, C.Y., et al., 2009. Characterization of a glycine N-methyltransferase gene knockout mouse model for hepatocellular carcinoma: implications of the gender disparity in liver cancer susceptibility. International Journal of Cancer 124:816–826.
[20] Liu, S.P., Li, Y.S., Lee, C.M., Yen, C.H., Liao, Y.J., Huang, S.F., et al., 2011. Higher susceptibility to aflatoxin B(1)-related hepatocellular carcinoma in glycine N-methyltransferase knockout mice. International Journal of Cancer 128:511–523.
[21] Varela-Rey, M., Martinez-Lopez, N., Fernandez-Ramos, D., Embade, N., Calvisi, D.F., Woodhoo, A., et al., 2010. Fatty liver and fibrosis in glycine N-methyltransferase knockout mice is prevented by nicotinamide. Hepatology 52:105–114.
[22] Madison, L.L., Lochner, A., Wulff, J., 1967. Ethanol-induced hypoglycemia. II. Mechanism of suppression of hepatic gluconeogenesis. Diabetes 16:252–258.
[23] Krebs, H.A., Freedland, R.A., Hems, R., Stubbs, M., 1969. Inhibition of hepatic gluconeogenesis by ethanol. Biochemical Journal 112:117–124.
[24] Luka, Z., Capdevila, A., Mato, J.M., Wagner, C., 2006. A glycine N-methyltransferase knockout mouse model for humans with deficiency of this enzyme. Transgenic Research 15:393–397.
[25] Ayala, J.E., Bracy, D.P., Malabanan, C., James, F.D., Ansari, T., Fueger, P.T., et al., 2011. Hyperinsulinemic-euglycemic clamps in conscious, unrestrained mice Journal of visualized experiments. JoVE.
[26] Hasenour, C.M., Wall, M.L., Ridley, D.E., Hughey, C.C., James, F.D., Wasserman, D.H., et al., 2015. Mass spectrometry-based microassay of (2)H and (13)C plasma glucose labeling to quantify liver metabolic fluxes in vivo. American Journal of Physiology. Endocrinology and Metabolism 309:E191–E203.
[27] Hughey, C.C., James, F.D., Bracy, D.P., Donahue, E.P., Young, J.D., Viollet, B., et al., 2017. Loss of hepatic AMP-activated protein kinase impedes the rate of glycogenolysis but not gluconeogenic fluxes in exercising mice. Journal of Biological Chemistry.
[28] Morgan, C.R., Lazarow, A., 1965. Immunoassay of pancreatic and plasma insulin following alloxan injection of rats. Diabetes 14:669–671.
[29] Soga, T., Heiger, D.N., 2000. Amino acid analysis by capillary electrophoresis electrospray ionization mass spectrometry. Analytical Chemistry 72:1236–1241.
[30] Soga, T., Ohashi, Y., Ueno, Y., Naraoka, H., Tomita, M., Nishioka, T., 2003. Quantitative metabolome analysis using capillary electrophoresis mass spectrometry. Journal of Proteome Research 2:488–494.
[31] Soga, T., Ueno, Y., Naraoka, H., Ohashi, Y., Tomita, M., Nishioka, T., 2002. Simultaneous determination of anionic intermediates for Bacillus subtilis metabolic pathways by capillary electrophoresis electrospray ionization mass spectrometry. Analytical Chemistry 74:2233–2239.
[32] Sugimoto, M., Wong, D.T., Hirayama, A., Soga, T., Tomita, M., 2010. Capillary electrophoresis mass spectrometry-based saliva metabolomics identified oral, breast and pancreatic cancer-specific profiles. Metabolomics 6:78–95.
[33] Hasenour, C.M., Ridley, D.E., James, F.D., Hughey, C.C., Donahue, E.P., Viollet, B., et al., 2017. Liver AMP-activated protein kinase is unnecessary for gluconeogenesis but protects energy state during nutrient deprivation. PLoS One 12:e0170382.
[34] Hirata, H., Sugimachi, K., Komatsu, H., Ueda, M., Masuda, T., Uchi, R., et al., 2016. Decreased expression of fructose-1,6-bisphosphatase associates with glucose metabolism and tumor progression in hepatocellular carcinoma. Cancer Research 76:3265–3276.
[35] Cho, J.H., Kim, G.Y., Mansfield, B.C., Chou, J.Y., 2018. Hepatic glucose-6-phosphatase-alpha deficiency leads to metabolic reprogramming in glycogen storage disease type Ia. Biochemical and Biophysical Research Communications 498:925–931.
[36] Mutel, E., Gautier-Stein, A., Abdul-Wahed, A., Amigo-Correig, M., Zitoun, C., Stefanutti, A., et al., 2011. Control of blood glucose in the absence of hepatic glucose production during prolonged fasting in mice: induction of renal and intestinal gluconeogenesis by glucagon. Diabetes 60:3121–3131.
[37] Rajas, F., Clar, J., Gautier-Stein, A., Mithieux, G., 2015. Lessons from new mouse models of glycogen storage disease type 1a in relation to the time course and organ specificity of the disease. Journal of Inherited Metabolic Disease 38:521–527.
[38] Martinez-Una, M., Varela-Rey, M., Cano, A., Fernandez-Ares, L., Beraza, N., Aurrekoetxea, I., et al., 2013. Excess S-adenosylmethionine reroutes phosphatidylethanolamine towards phosphatidylcholine and triglyceride synthesis. Hepatology 58:1296–1305.
[39] Liu, S.P., Li, Y.S., Chen, Y.J., Chiang, E.P., Li, A.F., Lee, Y.H., et al., 2007. Glycine N-methyltransferase-/- mice develop chronic hepatitis and glycogen storage disease in the liver. Hepatology 46:1413–1425.
[40] Zubiete-Franco, I., Garcia-Rodriguez, J.L., Martinez-Una, M., Martinez-Lopez, N., Woodhoo, A., Juan, V.G., et al., 2016. Methionine and S-

adenosylmethionine levels are critical regulators of PP2A activity modulating lipophagy during steatosis. Journal of Hepatology 64:409–418.

[41] Yang, J., Wang, C., Zhao, F., Luo, X., Qin, M., Arunachalam, E., et al., 2017. Loss of FBP1 facilitates aggressive features of hepatocellular carcinoma cells through the Warburg effect. Carcinogenesis 38:134–143.

[42] Yang, J., Jin, X., Yan, Y., Shao, Y., Pan, Y., Roberts, L.R., et al., 2017. Inhibiting histone deacetylases suppresses glucose metabolism and hepatocellular carcinoma growth by restoring FBP1 expression. Scientific Reports 7: 43864.

[43] Chen, R., Li, J., Zhou, X., Liu, J., Huang, G., 2017. Fructose-1,6-Bisphosphatase 1 reduces (18)F FDG uptake in hepatocellular carcinoma. Radiology 284:844–853.

[44] Fausto, N., Campbell, J.S., 2003. The role of hepatocytes and oval cells in liver regeneration and repopulation. Mechanisms of Development 120:117–130.

[45] Shiojiri, N., Lemire, J.M., Fausto, N., 1991. Cell lineages and oval cell progenitors in rat liver development Cancer research, vol. 51. p. 2611–20.

[46] Martinez-Chantar, M.L., Lu, S.C., Mato, J.M., Luka, Z., Wagner, C., French, B.A., et al., 2010. The role of stem cells/progenitor cells in liver carcinogenesis in glycine N-methyltransferase deficient mice. Experimental and Molecular Pathology 88:234–237.

[47] Christensen, C.E., Karlsson, M., Winther, J.R., Jensen, P.R., Lerche, M.H., 2014. Non-invasive in-cell determination of free cytosolic [NAD+]/[NADH] ratios using hyperpolarized glucose show large variations in metabolic phenotypes. Journal of Biological Chemistry 289:2344–2352.

[48] Pissios, P., 2017. Nicotinamide N-methyltransferase: more than a vitamin B3 clearance Enzyme. Trends in Endocrinology and Metabolism 28:340–353.

[49] Hong, S., Zhai, B., Pissios, P., 2018. Nicotinamide N-methyltransferase interacts with enzymes of the methionine cycle and regulates methyl Donor Metabolism. Biochemistry 57:5775–5779.

[50] Hong, S., Moreno-Navarrete, J.M., Wei, X., Kikukawa, Y., Tzameli, I., Prasad, D., et al., 2015. Nicotinamide N-methyltransferase regulates hepatic nutrient metabolism through Sirt1 protein stabilization. Nature Medicine 21: 887–894.

[51] Kraus, D., Yang, Q., Kong, D., Banks, A.S., Zhang, L., Rodgers, J.T., et al., 2014. Nicotinamide N-methyltransferase knockdown protects against diet-induced obesity. Nature 508:258–262.

[52] Brachs, S., Polack, J., Brachs, M., Jahn-Hofmann, K., Elvert, R., Pfenninger, A., et al., 2018. Genetic nicotinamide N-methyltransferase (Nnmt) deficiency in male mice improves insulin sensitivity in diet-induced obesity but does not affect glucose tolerance diabetes.

[53] Liao, Y.J., Chen, T.L., Lee, T.S., Wang, H.A., Wang, C.K., Liao, L.Y., et al., 2012. Glycine N-methyltransferase deficiency affects Niemann-Pick type C2 protein stability and regulates hepatic cholesterol homeostasis. Molecular Medicine 18:412–422.

[54] Bender, D.A., Olufunwa, R., 1988. Utilization of tryptophan, nicotinamide and nicotinic acid as precursors for nicotinamide nucleotide synthesis in isolated rat liver cells. British Journal of Nutrition 59:279–287.

[55] Liu, L., Su, X., Quinn 3rd, W.J., Hui, S., Krukenberg, K., Frederick, D.W., et al., 2018. Quantitative analysis of NAD synthesis-breakdown fluxes. Cell Metabolism 27:1067–1080 e1065.

[56] Badawy, A.A., 2017. Kynurenine pathway of tryptophan metabolism: regulatory and functional aspects. International Journal of Tryptophan Research 10, 1178646917691938.

[57] Tummala, K.S., Gomes, A.L., Yilmaz, M., Grana, O., Bakiri, L., Ruppen, I., et al., 2014. Inhibition of de novo NAD(+) synthesis by oncogenic URI causes liver tumorigenesis through DNA damage. Cancer Cell 26:826–839.

[58] Gomes, A.L., Teijeiro, A., Buren, S., Tummala, K.S., Yilmaz, M., Waisman, A., et al., 2016. Metabolic inflammation-associated IL-17a causes non-alcoholic steatohepatitis and hepatocellular carcinoma. Cancer Cell 30:161–175.

[59] Schuhwerk, H., Atteya, R., Siniuk, K., Wang, Z.Q., 2017. PARPing for balance in the homeostasis of poly(ADP-ribosyl)ation. Seminars in Cell & Developmental Biology 63:81–91.

[60] Houtkooper, R.H., Canto, C., Wanders, R.J., Auwerx, J., 2010. The secret life of NAD+: an old metabolite controlling new metabolic signaling pathways. Endocrine Reviews 31:194–223.

[61] Almeida, G.S., Bawn, C.M., Galler, M., Wilson, I., Thomas, H.D., Kyle, S., et al., 2017. PARP inhibitor rucaparib induces changes in NAD levels in cells and liver tissues as assessed by MRS. NMR Biomedicine 30.

[62] Mukhopadhyay, P., Horvath, B., Rajesh, M., Varga, Z.V., Gariani, K., Ryu, D., et al., 2017. PARP inhibition protects against alcoholic and non-alcoholic steatohepatitis. Journal of Hepatology 66:589–600.

[63] Batra, V., Kislay, B., 2013. Mitigation of gamma-radiation induced abasic sites in genomic DNA by dietary nicotinamide supplementation: metabolic up-regulation of NAD(+) biosynthesis. Mutation Research 749:28–38.

[64] Goodwin, P.M., Lewis, P.J., Davies, M.I., Skidmore, C.J., Shall, S., 1978. The effect of gamma radiation and neocarzinostatin on NAD and ATP levels in mouse leukaemia cells. Biochimica et Biophysica Acta 543:576–582.

[65] Skidmore, C.J., Davies, M.I., Goodwin, P.M., Halldorsson, H., Lewis, P.J., Shall, S., et al., 1979. The involvement of poly(ADP-ribose) polymerase in the degradation of NAD caused by gamma-radiation and N-methyl-N-nitrosourea. European Journal of Biochemistry 101:135–142.

[66] D'Amours, D., Desnoyers, S., D'Silva, I., Poirier, G.G., 1999. Poly(ADP-ribosyl)ation reactions in the regulation of nuclear functions. Biochemical Journal 342(Pt 2):249–268.

[67] Stincone, A., Prigione, A., Cramer, T., Wamelink, M.M., Campbell, K., Cheung, E., et al., 2015. The return of metabolism: biochemistry and physiology of the pentose phosphate pathway. Biological Reviews of the Cambridge Philosophical Society 90:927–963.

[68] De Santis, M.C., Porporato, P.E., Martini, M., Morandi, A., 2018. Signaling pathways regulating redox balance in cancer metabolism. Frontiers in oncology 8:126.

[69] Fan, J., Ye, J., Kamphorst, J.J., Shlomi, T., Thompson, C.B., Rabinowitz, J.D., 2014. Quantitative flux analysis reveals folate-dependent NADPH production. Nature 510:298–302.

[70] Kowalik, M.A., Columbano, A., Perra, A., 2017. Emerging role of the pentose phosphate pathway in hepatocellular carcinoma. Frontiers in oncology 7:87.

[71] Sato, E., Mori, T., Mishima, E., Suzuki, A., Sugawara, S., Kurasawa, N., et al., 2016. Metabolic alterations by indoxyl sulfate in skeletal muscle induce uremic sarcopenia in chronic kidney disease. Scientific Reports 6:36618.

[72] Lu, S.C., 2009. Regulation of glutathione synthesis Molecular aspects of medicine, vol. 30. p. 42–59.

[73] Lu, S.C., 2013. Glutathione synthesis. Biochimica et Biophysica Acta 1830: 3143–3153.

